Mechanisms for the transition to waviness for Taylor vortices

Denis Martinand, Eric Serre, and Richard M. Lueptow

Citation: Physics of Fluids (1994-present) **26**, 094102 (2014); doi: 10.1063/1.4895400
View online: http://dx.doi.org/10.1063/1.4895400
View Table of Contents: http://scitation.aip.org/content/aip/journal/pof2/26/9?ver=pdfcov
Published by the AIP Publishing

PHYSICS OF FLUIDS **26**, 094102 (2014)

Mechanisms for the transition to waviness for Taylor vortices

Denis Martinand,[1] Eric Serre,[1] and Richard M. Lueptow[2]
[1] *LM2P2 UMR 7340, Aix-Marseille Université/École Centrale Marseille/CNRS, IMT, La Jetée-Technopôle de Château-Gombert, 38 rue Frédéric Joliot-Curie, 13451 Marseille Cedex 20, France*
[2] *Department of Mechanical Engineering, Northwestern University, Evanston, Illinois 60208, USA*

(Received 11 March 2014; accepted 29 August 2014; published online 18 September 2014)

Building on the weakly nonlinear amplitude equation of the saturated Taylor vortices developing in a Taylor–Couette cell with a rotating inner cylinder and a fixed outer one, the physical mechanism underlying the destabilization of these vortices resulting in azimuthal waviness is addressed using Floquet analysis. For narrow gap configurations, analysis and direct numerical simulations together with existing experimental results support the idea that the waviness is generated by the axial shear in the azimuthal velocity due to the alternate advection by the Taylor vortices of azimuthal momentum between the cylinders. For wide gap configurations, this mechanism is no longer able to drive the azimuthal waviness and a different mechanism tends to select a subharmonic instability. © *2014 AIP Publishing LLC*. [http://dx.doi.org/10.1063/1.4895400]

I. INTRODUCTION

The transition from purely azimuthal (Couette) flow to counter-rotating toroidal (Taylor) vortices in the annulus between differentially rotating concentric cylinders represents one of the first successful applications of linear stability theory.[1] Focusing hereinafter on cases where the inner cylinder is rotating within a fixed outer cylinder, the instability, driven by the imbalance between the radial pressure gradient and the centripetal acceleration, is damped by viscosity at low angular velocities, but at higher angular velocities, the flow becomes unstable, resulting in Taylor vortices. The threshold is expressed in terms of a critical value of the rotating Reynolds number $\mathcal{R}e = \Omega r_{\mathrm{in}} d/\nu$, where Ω is the angular velocity of the inner cylinder, r_{in} its radius, $d = r_{\mathrm{out}} - r_{\mathrm{in}}$ the gap between the inner and outer cylinders, the radius of the latter being r_{out}, and ν the kinematic viscosity of the fluid. The pitchfork nature of the bifurcation and the exact analytical expression for the purely azimuthal base flow contribute to the excellent agreement of the experimental and numerical results with theoretical predictions (obtained by the numerical or analytical resolutions of the stability problem expressed as a one-dimensional differential eigen-problem, the eigen-values of which are the growth rates and the eigen-vectors of which are the radial shape functions) for the critical Reynolds number $\mathcal{R}e_{\mathrm{p}}^{\mathrm{crit}}$ above which this primary instability occurs at an associated critical axial wavenumber $k_{\mathrm{p}}^{\mathrm{crit}}$, which depend on the radius ratio $\eta = r_{\mathrm{in}}/r_{\mathrm{out}}$.[2] This agreement between experiments, numerics, and theory is further improved by taking into account the finite-length L of the system.[3]

While the mechanism driving the Taylor vortices has long been identified, the nature and dynamics of the next transition, in which the Taylor vortices acquire a waviness along the azimuthal direction, are less clear. Experimentally, the ratio of the secondary critical Reynolds number, above which waviness appears, to that for primary instability, $\epsilon_{\mathrm{s}}^{\mathrm{crit}} = \mathcal{R}e_{\mathrm{s}}^{\mathrm{crit}}/\mathcal{R}e_{\mathrm{p}}^{\mathrm{crit}}$, is between 1.12 and 1.31 for radius ratios $0.80 \leq \eta \leq 0.90$, depending on experimental conditions such as L, the length of the apparatus,[4–10] and related variations of the axial wavelength of the Taylor vortices.[11] In numerical simulations, to cite but a few, $\epsilon_{\mathrm{s}}^{\mathrm{crit}}$ as been reported to range from 1.26 to 1.74 for $\eta = 0.87$ and $L = 20d$ and $10d$, respectively,[8] and $\epsilon_{\mathrm{s}}^{\mathrm{crit}} = 1.32$ for $\eta = 0.85$ and $L = 20d$.[12] The number n_{s} of azimuthal waves in experiments is typically 2–7,[4] depending on the conditions by which the second transition is approached. Their azimuthal phase speed is, at mid-gap, 25%–50% of the inner cylinder surface speed for $0.80 \leq \eta \leq 0.90$, essentially independent of the observed n_{s}.[4,10,13–17] This phase speed is almost equal to the azimuthal velocity at the center of a vortex.[18] Small values of the radius ratio η are more seldom addressed but experiments and theory suggest that there is a sharp increase of $\epsilon_{\mathrm{s}}^{\mathrm{crit}}$ above $\sim$5 as η is decreased below 0.75.[11,13,19–22] Moreover, for specific acceleration procedures of the inner cylinder and $\eta \sim 0.7 - 0.75$, a disappearance of the azimuthal waviness and return to the axisymmetric Taylor Vortices has been observed as the Reynolds number is further increased above its critical value $\mathcal{R}e_{\mathrm{s}}^{\mathrm{crit}}$.[22,23]

One explanation for the transition to waviness relates to variations in the azimuthal flow resulting from radial transport of azimuthal momentum by Taylor vortices as noted by Davey *et al.*[24] and Jones.[20] Akonur and Lueptow[18] demonstrated experimentally that shear layers azimuthal velocity come about because Taylor vortices carry high azimuthal velocity fluid outward from the vicinity of the inner cylinder and low azimuthal velocity fluid inward from the vicinity of the outer cylinder. Taylor vortices hence build up azimuthal streaks of axially alternating high and low azimuthal velocity. The instability of the inflection points in the azimuthal velocity profile could then cause the transition to wavy vortex flow. This mechanism is thus akin to the dynamics and instability of longitudinal streaks observed in transitional shear flows such as boundary layers, plane Couette or channel flows.[25] Finlay *et al.*,[26] however, considering this mechanism in the context of Dean vortices, argued that this shear instability may not occur in Taylor–Couette flow because the shear layers are weaker. Marcus[16] speculated that an alternate physical mechanism in which a local, centrifugal instability of the radial outflow jet is responsible for the azimuthal waviness. This mechanism was based on the conversion of radial kinetic energy to azimuthal and axial kinetic energy upon the appearance of the traveling wave for $\eta = 0.875$. Finally, theoretical approaches of the second transition based on the competition between axisymmetric and nonaxisymmetric primary modes of instability implicitly assume that the centrifugal force also drives the dynamics of the waviness.[24,27–29] Thus, three candidates emerge as the physical mechanism driving the waviness. One is based on the centrifugal force (referred to as mechanism ① henceforth). Another is based on the shear associated with the variations along the axial direction of the radial velocity, or "radial jets" (mechanism ②). The last one is based on the shear associated with variations along the axial direction of the azimuthal velocity, or "azimuthal streaks" (mechanism ③). Here we provide theoretical insights on these different mechanisms, supported by results of numerical simulations and previous experiments.

The theoretical approach adopted here for the case of an inner cylinder rotating within a fixed outer cylinder involves secondary stability analysis of the base flow composed of the steady purely azimuthal flow combined with the saturated nonlinear state of the primary instability (Taylor vortices), obtained by a weakly nonlinear analysis.[30] More specifically, it is based on the third order amplitude equation of the primary instabilities and ignores slow spatial modulations along the axial direction. These modulations are related by Fourier transform to the band of linearly unstable axial wavenumbers that develops as the Reynolds number departs from its critical value. It will be therefore assumed here, for consistency with the amplitude equation, that the axial wavenumber of the primary instability remains at its critical value $k_{\mathrm{p}}^{\mathrm{crit}}$ whatever the value of the Reynolds number is. It is nonetheless clear that any change in this wavenumber quantitatively impacts the critical conditions of Taylor and wavy vortices. Since the primary instability is periodic in the axial direction, these secondary instabilities are sought as Floquet modes.[31] The specific terms associated with each of the aforementioned mechanisms can be selectively discarded in the operators involved in the secondary stability analysis. Thus, each mechanism can be removed individually from the linear dynamics of the secondary instability. The idea here is to isolate the necessary ingredient in the dynamics of the waviness, i.e., to identify which term triggers the waviness, by comparing the secondary instabilities obtained from the modified problems to that for the complete problem. This procedure differs from that used by Jones,[20] who compared the energies transferred by the different terms of the secondary dynamical equations to elucidate which one injects the highest amount of energy into this secondary instability. Moreover, complete dispersion relations of the Floquet modes are computed here in the form of the complex frequency ω_{s} as functions of the Reynolds number $\mathcal{R}e$

and axial and azimuthal secondary wavenumbers k_s and n_s, respectively. The complex frequencies of the secondary modes are characterized by their growth rates, i.e., their imaginary parts $\mathrm{Im}(\omega_s)$, and the azimuthal phase speed at mid-gap $v_\phi = (\mathrm{Re}\,(\omega_s)\,(r_{\mathrm{out}} + r_{\mathrm{in}}))\,/\,(2n_s\mathcal{R}e)$. Striking changes in the graphical representations of the growth rate and phase speed of the most unstable mode can then be related to a switch between modes of different types, e.g., modes presenting strongly different shape functions and possibly driven by different mechanisms.

Combined with this analytical approach, previous experimental data have been reexamined and dedicated numerical simulations have been performed. The analytical method is described in Sec. II and its results, together with specific numerical and experimental results, pertaining to the secondary transition for η ranging from 0.97 down to 0.50 are presented and discussed in Sec. III.

II. ANALYTICAL AND NUMERICAL APPROACHES

In a classical fashion, an infinitely long annular cavity filled with a Newtonian fluid is considered. Using cylindrical coordinates $(r,\ \theta,\ z)$, the radial, azimuthal, and axial components of the velocity field $\boldsymbol{V} = (U, V, W)^t$ and the pressure-over-density field $Q = P/\rho$ satisfy the continuity and incompressible, three-dimensional Navier-Stokes equations. Velocities are made nondimensional by Ωr_{in}, lengths by the gap d, times by d^2/ν, and Q by $\Omega^2 r_{\mathrm{in}}^2$ so that all quantities are henceforth nondimensional. Surfaces are no-slip, and impermeable boundary conditions are satisfied on the nondimensional inner and outer radii: $U\left(r_{\mathrm{in/out}}, \theta, z\right) = V\left(r_{\mathrm{out}}, \theta, z\right) = W\left(r_{\mathrm{in/out}}, \theta, z\right) = 0$ and $V\left(r_{\mathrm{in}}, \theta, z\right) = 1$. The solution for the purely azimuthal flow is $\boldsymbol{V}_l\,(r) = \boldsymbol{v}_l\,(r) = \left(0, \left(r_{\mathrm{in}} r_{\mathrm{out}}^2 - r_{\mathrm{in}} r^2\right) / \left(r r_{\mathrm{out}}^2 - r r_{\mathrm{in}}^2\right), 0\right)^t$, together with the associated pressure field. Throughout the paper, capital $\boldsymbol{V}\,(r, \theta, z) = (U, V, W)^t$ and $\boldsymbol{X}\,(r, \theta, z) = (U, V, W, Q)^t$ denote the velocity and velocity–pressure fields as functions of r, θ, and z, while smaller case $\boldsymbol{v}\,(r) = (u, v, w)^t$ and $\boldsymbol{x}\,(r) = (u, v, w, q)^t$ refer to the radial shape functions of these fields.

The stability of the purely azimuthal flow with respect to small perturbations is addressed by linear stability analysis. As the Reynolds number is increased above a critical value $\mathcal{R}e_{\mathrm{p}}^{\mathrm{crit}}$ the flow becomes unstable. This primary instability takes the form of a stack of toroidal counter-rotating (Taylor) vortices, $\boldsymbol{V}_{\mathrm{p}}\,(r, z) = A\boldsymbol{v}_{\mathrm{p}}^{\mathrm{crit}}(r) \times \exp(\mathrm{i}k_{\mathrm{p}}^{\mathrm{crit}} z) + \mathrm{c.c.}$, where the amplitude A remains arbitrary at this linear stage and is assumed to be small.

The saturated nonlinear states of the primary instabilities are obtained by a weakly nonlinear analysis, leading to the equation satisfied by amplitude A,[30]

$$\frac{\partial A}{\partial t} = \left.\frac{\partial \sigma_{\mathrm{p}}}{\partial \mathcal{R}e}\right|^{\mathrm{crit}} \left(\mathcal{R}e - \mathcal{R}e_{\mathrm{p}}^{\mathrm{crit}}\right) A + \mu A^2 \overline{A}, \tag{1}$$

where σ_{p} is the growth rate of the primary instability. As the present study does not consider effects associated with a finite axial extension, the amplitude (Stuart–Landau) equation (1) does not include the term associated with slow spatial variations of A along the axial direction which would be found in the corresponding envelope (Ginzburg–Landau) equation. Consequently, A does not introduce any spatial variations in the form of axial boundary conditions or shifts of the axial wavenumber, which remains at its value $k_{\mathrm{p}}^{\mathrm{crit}}$ selected at critical conditions. Moreover, the radial shape functions $\boldsymbol{v}_{\mathrm{p}}^{\mathrm{crit}}(r)$ also conserve their values computed at critical conditions. The weakly nonlinear analysis also yields an expansion of the velocity field of the perturbation that contains two nonlinear terms: one adding up to the purely azimuthal flow, the other generating a first harmonic of the primary instability. The new base flow to be used for the secondary stability analysis then reads

$$\boldsymbol{V}_b\,(r, z; \mathcal{R}e) = \boldsymbol{v}_0(r) + \left[\boldsymbol{v}_1 \times \exp\left(\mathrm{i}k_{\mathrm{p}}^{\mathrm{crit}} z\right) + \mathrm{c.c.}\right] + \left[\boldsymbol{v}_2 \times \exp\left(\mathrm{i}k_{\mathrm{p}}^{\mathrm{crit}} z\right) + \mathrm{c.c.}\right], \tag{2}$$

where $\boldsymbol{v}_0 = \boldsymbol{v}_l\,(r) + A^2\boldsymbol{v}_{nl,0}(r)$ combines the purely azimuthal flow and the non-oscillating nonlinear correction, $\boldsymbol{v}_1 = A\boldsymbol{v}_{\mathrm{p}}^{\mathrm{crit}}(r)$ is the nonlinearly saturated primary instability, and $\boldsymbol{v}_2 = A^2\boldsymbol{v}_{nl,2}(r)$ is the radial dependence of the first harmonic nonlinear correction. Owing to the stationary nature of the Taylor vortices, the coefficients $\partial_{\mathcal{R}e}\sigma_{\mathrm{p}}$ and μ in (1) are real. Together with the radial shape functions $\boldsymbol{v}_{nl,0}(r)$ and $\boldsymbol{v}_{nl,2}(r)$, they are computed as outcomes of the linear stability problem and expansions of the velocity field and Navier–Stokes equation in powers of $(\mathcal{R}e - \mathcal{R}e_{\mathrm{p}}^{\mathrm{crit}})$ in a standard fashion.

The amplitude at saturation is then obtained from the stationary solution of (1) as a function of $\mathcal{R}e$: $A = \sqrt{\partial_{\mathcal{R}e}\sigma_{\mathrm{p}}^{\mathrm{crit}}(\mathcal{R}e - \mathcal{R}e_{\mathrm{p}}^{\mathrm{crit}})/\mu}$. Albeit an approximation, (2) contains the two key ingredients to drive the dynamics of secondary instabilities: the nonlinear modification of the base flow, $\boldsymbol{v}_{nl,0}$, is expected to restabilize the azimuthal velocity profile $\boldsymbol{v}_l$ and the primary instability is expected to result in new mechanisms of secondary instability.

According to Floquet analysis,[31] the solution for the secondary instability is sought as

$$\boldsymbol{X}_{\mathrm{s}} = \sum_{j=-\infty}^{\infty} \boldsymbol{x}_{\mathrm{s},j}(r) \times \exp\left(\mathrm{i} j k_{\mathrm{p}}^{\mathrm{crit}} z\right) \times \exp\left(\mathrm{i}k_{\mathrm{s}}z + \mathrm{i}n_{\mathrm{s}}\phi - \mathrm{i}\omega_{\mathrm{s}}t\right) + \mathrm{c.c.} \tag{3}$$

Combining (2) and (3) after truncating the periodic Floquet vectors up to the lth first harmonics, inserting them in the Navier-Stokes and continuity equations, and linearizing the equations about the base state (2) yields a system of equations, written in a condensed manner as a generalized eigenproblem leading to the complex eigenvalue ω_{s} associated with eigenvectors $\boldsymbol{x}_{\mathrm{s}} = (u_{\mathrm{s},-l}, \ldots, u_{\mathrm{s},l}, v_{\mathrm{s},-l}, \ldots, v_{\mathrm{s},l}, w_{\mathrm{s},-l}, \ldots, w_{\mathrm{s},l}, q_{\mathrm{s},-l}, \ldots, q_{\mathrm{s},l},)^t$:

$$\mathcal{A}\boldsymbol{x}_{\mathrm{s}} - \mathrm{i}\omega_{\mathrm{s}}\mathcal{B}\boldsymbol{x}_{\mathrm{s}} = \boldsymbol{0}. \tag{4}$$

With $\boldsymbol{v}_0$ and $\boldsymbol{v}_1$ in (2), the $(4 \times (2l + 1)) \times (4 \times (2l + 1))$ operator matrix $\mathcal{A}$ is

$$\mathcal{A}\left(k_{\mathrm{s}}, n_{\mathrm{s}}, \mathrm{Ta}; k_{\mathrm{p}}^{\mathrm{crit}}, \boldsymbol{v}_0, \boldsymbol{v}_1, \boldsymbol{v}_2\right) = \tag{5}$$

$$\begin{bmatrix}
\begin{array}{c}\boxed{\mathcal{D}_u^+ d_r}_{\text{②}} + \mathcal{D}_{d_r u}^+ + \\ \boxed{\mathrm{i}r^{-1}\mathcal{D}_v^+ n_{\mathrm{s}}}_{\text{③}} + \mathrm{i}\mathcal{D}_w^+\mathcal{K} \\ -\mathcal{R}e^{-1}\left(\Delta - r^{-2}\mathcal{I}\right)\end{array} &
\begin{array}{c}\boxed{-2r^{-1}\mathcal{D}_v^+}_{\text{①}} \\ +2\mathrm{i}\mathcal{R}e^{-1}r^{-2}\mathcal{I}n_{\mathrm{s}}\end{array} &
\boxed{\mathrm{i}\mathcal{D}_u^- k_{\mathrm{p}}^{\mathrm{crit}}}_{\text{②}} &
d_r\mathcal{I} \\
\begin{array}{c}\mathcal{D}_{d_r v}^+ + r^{-1}\mathcal{D}_v^+ \\ -2\mathrm{i}\mathcal{R}e^{-1}r^{-2}\mathcal{I}n_{\mathrm{s}}\end{array} &
\begin{array}{c}\boxed{\mathcal{D}_u^+ d_r}_{\text{②}} + r^{-1}\mathcal{D}_u^+ + \\ \boxed{\mathrm{i}r^{-1}\mathcal{D}_v^+ n_{\mathrm{s}}}_{\text{③}} + \mathrm{i}\mathcal{D}_w^+\mathcal{K} \\ -\mathcal{R}e^{-1}\left(\Delta - r^{-2}\mathcal{I}\right)\end{array} &
\boxed{\mathrm{i}\mathcal{D}_v^- k_{\mathrm{p}}^{\mathrm{crit}}}_{\text{③}} &
\mathrm{i}r^{-1}\mathcal{I}n_{\mathrm{s}} \\
\mathcal{D}_{d_r w}^+ &
0 &
\begin{array}{c}\boxed{\mathcal{D}_u^+ d_r}_{\text{②}} + \\ \boxed{\mathrm{i}r^{-1}\mathcal{D}_v^+ n_{\mathrm{s}}}_{\text{③}} \\ +\mathrm{i}\left(\mathcal{D}_w^+\mathcal{K} + \mathcal{D}_w^- k_{\mathrm{p}}^{\mathrm{crit}}\right) \\ -\mathcal{R}e^{-1}\Delta\end{array} &
\mathrm{i}\mathcal{K} \\
d_r\mathcal{I} + r^{-1}\mathcal{I} &
\mathrm{i}r^{-1}\mathcal{I}n_{\mathrm{s}} &
\mathrm{i}\mathcal{K} &
0
\end{bmatrix},$$

where d_r is the derivative with respect to r. In addition to the identity $\mathcal{I}$, $(2l + 1) \times (2l + 1)$ operators applying to each of the four physical components of $\boldsymbol{x}_{\mathrm{s}}$ are introduced and their respective (i, j) coefficients given by:

- $\mathcal{D}^+_{v\,i,j} = v_0\delta_{i,j} + v_1\delta_{i,j+1} + \overline{v_1}\delta_{i,j-1} + v_2\delta_{i,j+2} + \overline{v_2}\delta_{i,j-2}$ and $\mathcal{D}^-_{v\,i,j} = v_1\delta_{i,j+1} - \overline{v_1}\delta_{i,j-1} + v_2\delta_{i,j+2} - \overline{v_2}\delta_{i,j-2}$, where v_n stands for one of the components of $\boldsymbol{v}_n$ and $\overline{v_n}$ for its complex conjugate, and $\delta_{i,j}$ is the Kronecker delta. These operators account for advective terms: the advection of $\boldsymbol{v}_{\mathrm{s}}$ by the base flow (2) for $\mathcal{D}_v^+$ and the reciprocal for $\mathcal{D}_v^-$.
- $\mathcal{K}_{i,j} = \delta_{i,j}\left(k_{\mathrm{s}} + (j - l - 1)\, k_{\mathrm{p}}^{\mathrm{crit}}\right)$ for the axial wavenumbers of modes (3).
- $\Delta = d_r^2\mathcal{I} + 1/r d_r\mathcal{I} - 1/r^2\mathcal{I}^2 n_{\mathrm{s}}^2 - \mathcal{K}^2$ for the Laplacian in cylindrical coordinates.

The matrix $\mathcal{B}$ is the identity multiplied by $\mathcal{R}e^{-1}$, applied to the components of the velocity. The radial shape functions are then expanded over n Chebyshev polynomials, and problem (4) is solved by spectral method, setting $n = 14$ and $l = 7$, values for which a satisfying accuracy is reached. The solution of (4) and the selection of the most unstable (or least stable) mode leads to the secondary dispersion relation for this mode in the form $\omega_{\mathrm{s}}\,(\mathcal{R}e, k_{\mathrm{s}}, n_{\mathrm{s}})$, from which the growth rate, $\mathrm{Im}(\omega_{\mathrm{s}})$, and the azimuthal phase speed at mid-gap $r_{\mathrm{mid}} = (r_{\mathrm{out}} + r_{\mathrm{in}})/2$, $v_\phi = (\mathrm{Re}\,(\omega_{\mathrm{s}})\, r_{\mathrm{mid}})\,/\,(n_{\mathrm{s}}\mathcal{R}e)$, are readily obtained (note that, to conform with previous convention, this phase speed is made non-dimensional by the speed of the inner cylinder). The growth rates $\mathrm{Im}(\omega_{\mathrm{s}})$ are invariant by the changes $k_{\mathrm{s}} \to \pm k_{\mathrm{s}} + m k_{\mathrm{p}}^{\mathrm{crit}}$, with $m \in \mathbb{Z}$ and $n_{\mathrm{s}} \to -n_{\mathrm{s}}$, so the secondary stability analysis is restricted to $0 \leq k_{\mathrm{s}} \leq k_{\mathrm{p}}^{\mathrm{crit}}/2$ and $n_{\mathrm{s}} \geq 0$. Moreover, the critical secondary condition $\left(\mathcal{R}e_{\mathrm{s}}^{\mathrm{crit}}, k_{\mathrm{s}}^{\mathrm{crit}}, n_{\mathrm{s}}^{\mathrm{crit}}\right)$, i.e., the Reynolds number above which a secondary mode (3) with $k_{\mathrm{s}} = k_{\mathrm{s}}^{\mathrm{crit}}$ and $n_{\mathrm{s}} = n_{\mathrm{s}}^{\mathrm{crit}}$ first becomes unstable are obtained by a Newton–Raphson method iterating so as to reach $\mathrm{Im}\left(\omega_{\mathrm{s}}\left(\mathcal{R}e_{\mathrm{s}}^{\mathrm{crit}}, k_{\mathrm{s}}^{\mathrm{crit}}, n_{\mathrm{s}}^{\mathrm{crit}}\right)\right) = 0$ and $\partial_{k_{\mathrm{s}}}\mathrm{Im}\left(\omega_{\mathrm{s}}\left(\mathcal{R}e_{\mathrm{s}}^{\mathrm{crit}}, k_{\mathrm{s}}^{\mathrm{crit}}, n_{\mathrm{s}}^{\mathrm{crit}}\right)\right) = 0$.

Numerical simulations used to provide additional insight into the flow utilize a multi-domain pseudo-spectral method based on Chebyshev polynomials in the radial and axial directions and Fourier modes in the azimuthal ones. Time integration is accomplished with a second-order backward implicit Euler scheme for the linear terms and a second-order explicit Adams-Bashforth scheme for the nonlinear terms.[32] An improved projection algorithm is employed for velocity-pressure coupling.[33] The continuity between the subdomains of the velocity and pressure fields is enforced using an influence matrix technique.[34] Rigid and impermeable conditions are implemented on all walls. Moreover, the axial end-wall disks rotate at the rate of the inner cylinder. In each subdomain, the mesh grid is defined by the Gauss–Lobatto–Chebyshev collocation points, with $n_r = 21$ and $n_z = 21$ points in the radial and axial directions, respectively. For three-dimensional non-axisymmetric simulations, $n_\phi = 16$ equally spaced mesh points are used in the azimuthal direction. The code has been verified with respect to a manufactured solution (i.e., a synthetic analytical solution satisfying the Navier–Stokes equation to which an *ad hoc* body force term has been added),[34] and a mono-domain version has been extensively validated in Taylor–Couette configurations.[12,35] The simulations use 20 axial subdomains in order to improve the speed of the computations. More importantly, this also allows us to perform numerical simulations at high values for the aspect ratio $L/d = 50$ in order to alleviate the strong damping effect of axial confinement on the azimuthal waviness.

III. MECHANISMS FOR WAVINESS

In operator (5), the term ① combined with v_{s} is the linearized centrifugal force, or linearized centripetal acceleration. The terms ② combined with $\boldsymbol{v}_{\mathrm{s}}$ are the linearized advection terms associated with the axial shear in the radial velocity. The terms ③ combined with $\boldsymbol{v}_{\mathrm{s}}$ are the linearized advection terms associated with the axial shear in the azimuthal velocity. Terms ② and ③ are akin to the advection terms found in the Orr–Sommerfeld equation. The stability analysis of the most unstable mode resulting from the modified dispersion relations pertaining to cases ①, ②, or ③, where the two complementary terms among ①, ②, or ③ in the $\mathcal{A}$ operator (5) are omitted, can be compared to the analysis using the complete $\mathcal{A}$.

A. Narrow gap (large η) case

The comparison between the solution with the complete operator and the three cases is shown in Figure 1 for the growth rate and Figure 2 for the azimuthal phase speed (when relevant) for $\eta = 0.85$, where $\mathcal{R}e_{\mathrm{p}}^{\mathrm{crit}} = 108.31$ and $k_{\mathrm{p}}^{\mathrm{crit}} = 3.13$. For the sake of clarity, $\mathrm{Im}(\omega_{\mathrm{s}})$ and v_ϕ are plotted for the value of the azimuthal wavenumber $n_{\mathrm{s}} = n_{\mathrm{s}}^{\mathrm{max}}\,(\mathcal{R}e, k_{\mathrm{s}})$ with the highest growth rate.

Some obvious features of the natural secondary instability are evident in Figures 1(a) and 2(a), which include the entire operator $\mathcal{A}$. There is a "harmonic ridge," centered on $k_{\mathrm{s}} = 0$, the value for which the secondary modes exhibit the axial periodicity of the primary mode, with increasing azimuthal wavenumber, n_{s}, as $\mathcal{R}e$ increases. This selection of the azimuthal wavenumber is actually very tenuous, the growth rates along the "harmonic ridge" being only weakly dependent on n_{s}. This ridge emerges from an "axisymmetric plain," where secondary modes are axisymmetric ($n_{\mathrm{s}} = 0$) and stable ($\mathrm{Im}(\omega_{\mathrm{s}}) < 0$). Moreover, a "subharmonic hill" centered on $k_{\mathrm{s}} = k_{\mathrm{p}}^{\mathrm{crit}}/2 = 1.56$, the value for which the axial wavelength of the secondary modes double the primary one, also emerges for

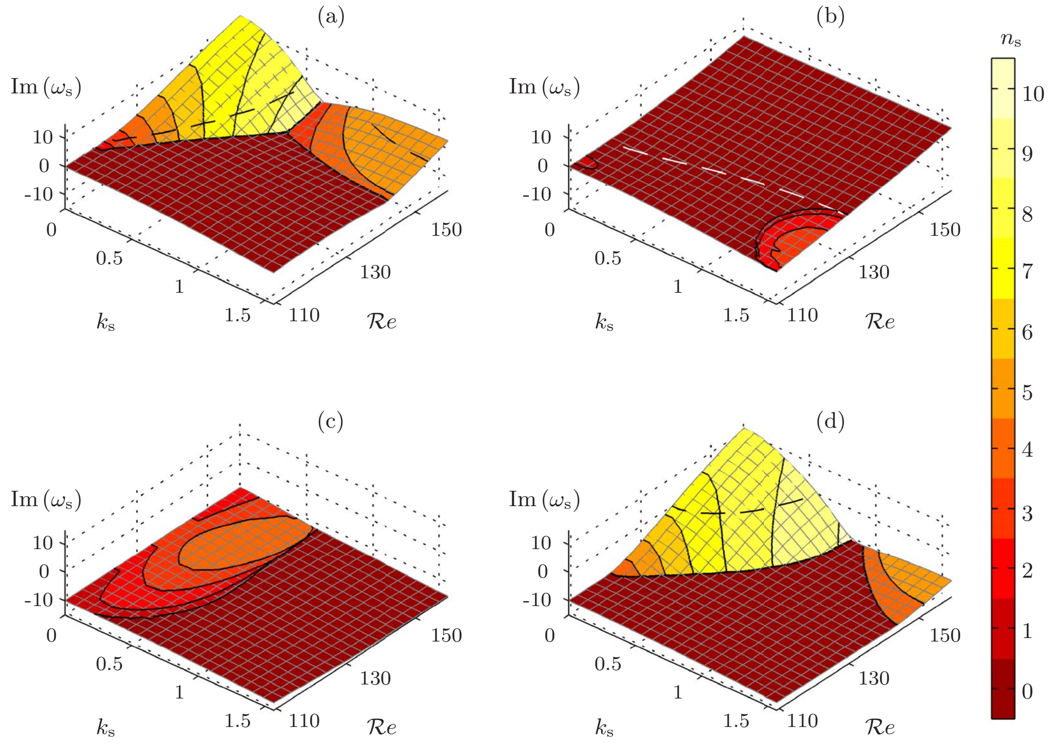

FIG. 1. Growth rate $\mathrm{Im}(\omega_\mathrm{s})$ and azimuthal wavenumber n_s (colorscale) of the secondary instability, as a function of the Floquet axial wavenumber k_s and Reynolds number Ta, for $\eta = 0.85$. The dashed lines locate the marginal $\mathrm{Im}(\omega_\mathrm{s}) = 0$ conditions. (a) Complete operator $\mathcal{A}$ (b) Case ①, azimuthal and radial shears removed from $\mathcal{A}$. (c) Case ②, azimuthal shear and centrifugal force removed from $\mathcal{A}$. (d) Case ③, radial shear and centrifugal force removed from $\mathcal{A}$.

$\mathcal{R}e > 150$, for nonaxisymmetric and stable modes. The azimuthal phase speed on the "harmonic ridge" remains close to 0.5 for all n_s or $\mathcal{R}e$, while it is substantially smaller on the "subharmonic hill," where, moreover, its sign become negative as $\mathcal{R}e$ increases. Considering the marginal curves in Figure 1(a), critical conditions ($\mathrm{Im}(\omega_\mathrm{s}) = 0$) are reached on the "harmonic ridge" for $\mathcal{R}e_\mathrm{s}^\mathrm{crit} = 121.2$, i.e., $\epsilon_\mathrm{s}^\mathrm{crit} = 1.12$, and $n_\mathrm{s}^\mathrm{crit} = 3$, with $v_\phi^\mathrm{crit} = 0.50$. This is consistent with previous theoretical values of $\epsilon_\mathrm{s}^\mathrm{crit} = 1.17$, $n_\mathrm{s}^\mathrm{crit} = 3$, and $v_\phi^\mathrm{crit} = 0.48$ for $\eta = 0.87$ and infinitely long cylinders[8] and with present numerical simulations values of $1.11 < \epsilon_\mathrm{s}^\mathrm{crit} < 1.20$ and $n_\mathrm{s}^\mathrm{crit} = 3$ for $\eta = 0.85$ and a length to gap ratio of $L/d = 50$. Numerical simulation results for these wavy vortices just above their threshold are depicted in Figure 3 together with corresponding analytical results. The wavy vortices can be observed in the numerical simulations in the central region, but the axial end-walls extend their influence, evident as diminished waviness, over almost one-fourth of the domain at each end.

Comparing these features with the ones in (b), (c), and (d) of Figures 1 and 2, the only case obviously close to the complete dispersion relation of Figures 1(a) and 2(a) is the one pertaining to the azimuthal streaks, depicted in Figures 1(d) and 2(d). This comparison is supported by three specific features: (1) the rise of a harmonic instability associated with the "ridge" at $k_\mathrm{s} = 0$; (2) the fact that this instability selects a secondary mode with $n_\mathrm{s} \neq 0$; and (3) a similar azimuthal phase speed. Moreover, the presence of "subharmonic hill" in Figure 1(a) is also retrieved by mechanism ③. The centrifugal term alone in Figure 1(b) drives an axisymmetric instability. The radial jets alone in Figure 1(c) do not drive any instability, though the least stable modes are nonaxisymmetric. Moreover, phase speeds in the two last cases remain very small positive or negative quantities as shown in Figures 2(b) and 2(c). The "axisymmetric plain" recovers the mechanism driving the Taylor vortices, amplified by the centrifugal force and damped by viscosity. Without the centrifugal force term ①, the "axisymmetric plain" is stable in Figures 1(c) and 1(d). We also extrapolate from the higher overall growth rate in Figure 1(a) compared to Figure 1(d) that the centrifugal term enhances

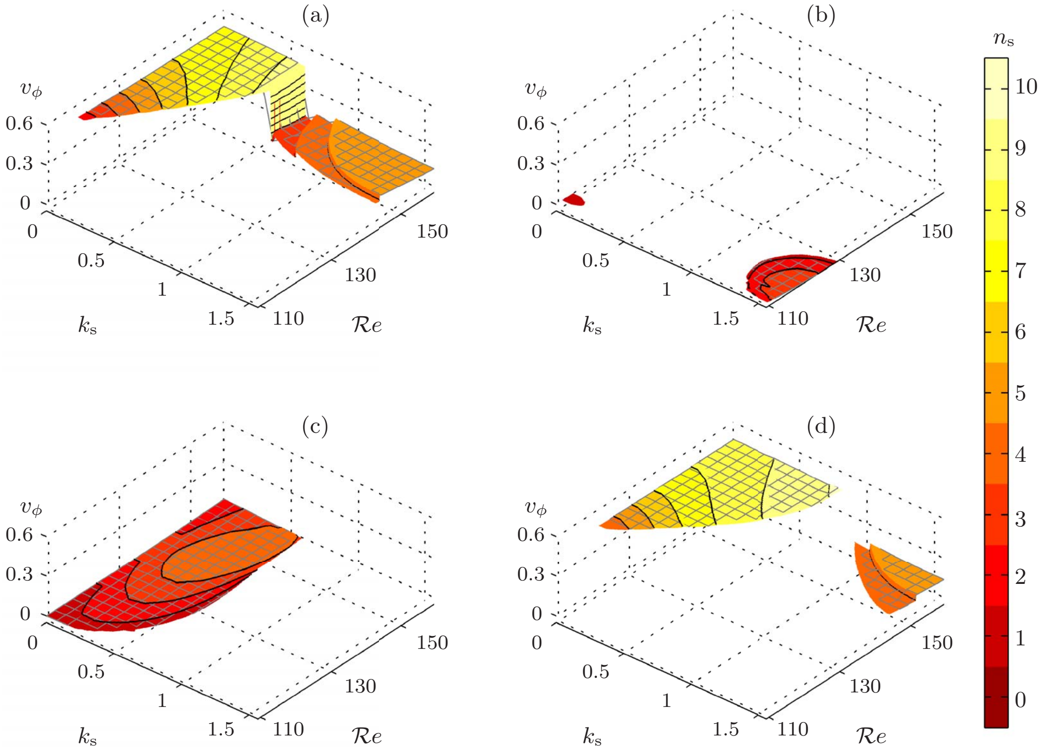

FIG. 2. Phase speed at mid-gap $v_\phi = \mathrm{Re}\,(\omega_s)\, r_{\mathrm{mid}}/\,(n_s \mathcal{R}e)$ and azimuthal wavenumber n_s (colorscale) of the secondary instability, as a function of the Floquet axial wavenumber k_s and Reynolds number Ta, for $\eta = 0.85$. (a)–(d) as in Figure 1.

the instabilities associated with mechanism ③. Although quantitative results (specific values for $\mathcal{R}e_s^{\mathrm{crit}}$, n_s^{crit}, and v_ϕ^{crit}) should be considered with caution owing to the weakly nonlinear approach of the primary instability and the sensitivity of the secondary stability analysis with respect to the base flow, qualitative similarities between the complete dispersion relation and results for azimuthal streaks (case ③) unambiguously show the dominance of a secondary instability mechanism driven by the axial shear in the azimuthal velocity.

Experimental and numerical results further support this idea. The shear layers related to the azimuthal streaks are conspicuous in experimental and numerical azimuthal velocity vector plots (see Figure 9 of Ref. 18 or Figure 4 of Ref. 8), and they stretch around the entire circumference of the Taylor–Couette cell. The predominance of the azimuthal streaks is confirmed by numerical simulations. By forcing axisymmetric fields in the numerics, non-wavy Taylor vortices can be artificially maintained even above the threshold for wavy secondary instabilities. The amplitudes of the axial shears at mid gap in the radial (radial jets) and azimuthal (azimuthal streaks) velocity profiles are compared for $\mathcal{R}e = 110$, 120, and 140, corresponding to $\epsilon = \mathcal{R}e/\mathcal{R}e_p^{\mathrm{crit}} = 1.02$, 1.11, and 1.29, respectively, in Figure 4. The axial shear of the azimuthal velocity is about three times larger than that for the radial velocity, regardless of the value for ϵ, consistent with the azimuthal streaks, not the radial jets, driving the transition to wavy vortices.

The azimuthal shear layers are expected to sustain Kelvin–Helmholtz-like instabilities. Two features of such instabilities, inferred from Rayleigh's stability equation, are of interest. First, this inviscid stability analysis of plane shear flows indicates that all wavelengths along the direction of the flow are unstable, so the preferred wavelength of the Kelvin–Helmholtz instabilities, if there is one, is determined by viscous or geometric effects. It is known that for wavy vortex flow, a variety of azimuthal wavelengths can occur. Between two and four waves are typical, though sometimes more appear,[4] depending on startup and other conditions. That the number of waves, and hence the wavelength, can vary depending on experimental details and that the wavelength adjusts so there are an integer number of waves around the circumference of the annulus are both consistent

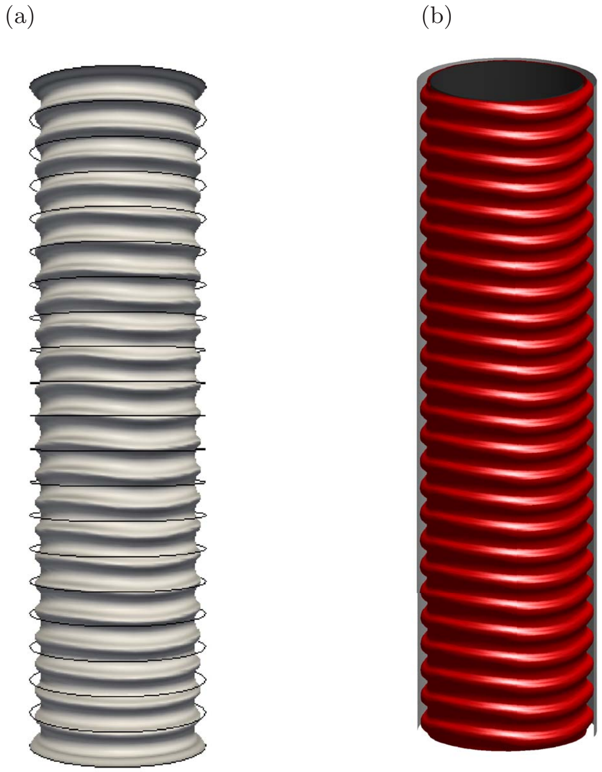

FIG. 3. Isosurfaces $V = 0.5$ of the azimuthal velocity ($V = 1$ on the rotating inner cylinder) for radius ratio $\eta = 0.85$ at $\mathcal{R}e = 130$. (a) Numerical simulation with aspect ratio $L/d = 50$. (b) Corresponding analytical isosurface obtained from expressions (2) and (3) at critical conditions $\left(\mathcal{R}e_{\rm s}^{\rm crit}, k_{\rm s}^{\rm crit}, n_{\rm s}^{\rm crit}\right)$, with an arbitrary amplitude for the azimuthal waviness.

with the idea that the mechanism of instability supports all wavelengths. Second, the inviscid Kelvin–Helmholtz wave travels at a phase speed equal to the average of the two velocities generating the shear layer, V_1 and V_2, such that the estimated phase speed is $0.5\,(V_1 + V_2)$. For wavy vortex flows, the azimuthal phase speed of the waves can be extracted from previous experimental data. Contours of the azimuthal velocity profile in Figure 7 of Ref. (18) allow the estimation of the maximum and minimum azimuthal velocity at mid-gap V_1 and V_2 for three different values of $\epsilon = 1.28$, 2.48, and 5.03 for $\eta = 0.81$. Obtaining $V_1 = 0.25$, 0.24, and 0.23 and $V_2 = 0.61$, 0.54, and 0.47, it is then possible to compare $0.5\,(V_1 + V_2) = 0.43$, 0.39, and 0.35 to the measured values $v_\phi = 0.44$, 0.36, and 0.30. While the match is imperfect, the error is relatively small and could be accounted for

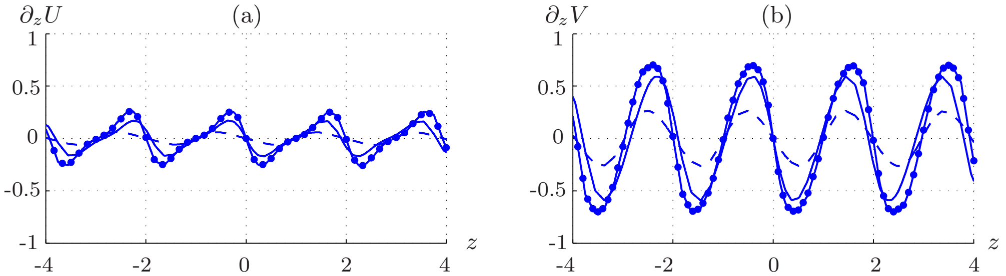

FIG. 4. Axial variations of the dimensionless axial shears of the radial (a) and azimuthal (b) velocities at mid-gap $r_{\rm mid} = (r_{\rm out} + r_{\rm in})/2$, obtained from numerical simulations for $\eta = 0.85$, at Reynolds numbers $\mathcal{R}e = 110$ (dashed lines), 120 (solid lines) and 140 (solid lines with dots). Note that $\mathcal{R}e_{\rm p}^{\rm crit} = 108.31$. While the full axial extension of the numerical domain is $-25 < z < 25$, only the central part $-4 < z < 4$ is shown.

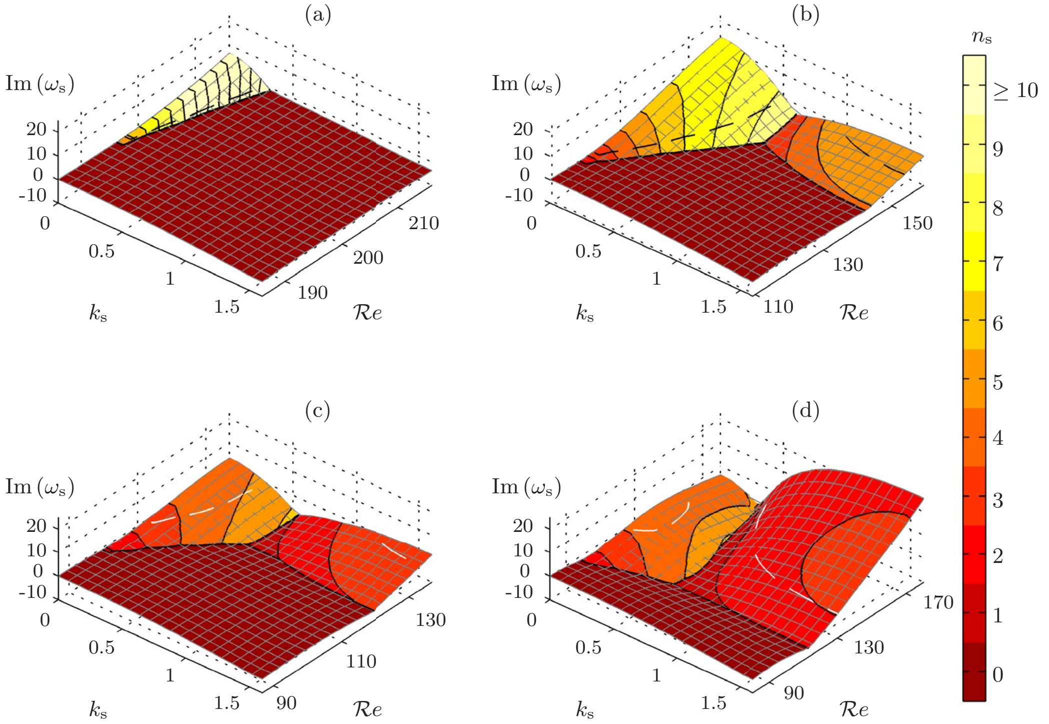

FIG. 5. Growth rate Im(ω_s) and azimuthal wavenumber n_s (colorscale up to $n_s = 10$) of the secondary instability, as a function of the Floquet axial wavenumber k_s and Reynolds number Ta for the complete operator $\mathcal{A}$, (a) $\eta = 0.95$, leading to $\mathcal{R}e_s^{\text{crit}} = 195.5$, $\epsilon_s^{\text{crit}} = 1.06$, $n_s = 4$, and $v_\phi = 0.52$ (note that azimuthal wavenumbers between $n_s = 10$ and 17 share the same color and are distinguished by the solid lines only). (b) $\eta = 0.85$, leading to $\mathcal{R}e_s^{\text{crit}} = 121.2$, $\epsilon_s^{\text{crit}} = 1.12$, $n_s = 3$, and $v_\phi = 0.50$. (c) $\eta = 0.75$, leading to $\mathcal{R}e_s^{\text{crit}} = 111.8$, $\epsilon_s^{\text{crit}} = 1.30$, $n_s = 3$, and $v_\phi = 0.44$. (d) $\eta = 0.7$, leading to $\mathcal{R}e_s^{\text{crit}} = 125.0$, $\epsilon_s^{\text{crit}} = 1.57$, $n_s = 4$, and $v_\phi = 0.35$. The dashed lines locate the marginal Im(ω_s) = 0 conditions. Note the smaller range of Reynolds numbers for $\eta = 0.95$ and the larger range for $\eta = 0.7$.

by the curvature of the vortex flow and the viscosity. Furthermore, both the estimated phase speed $0.5\,(V_1 + V_2)$ and measured one v_ϕ decrease as the Reynolds number increases.

Figure 5 shows that the "harmonic ridge" persists in plots of Im(ω_s) for $0.7 \leq \eta \leq 0.95$, while the "subharmonic hill" disappears for $\eta = 0.95$, at least in the depicted Reynolds number range $\mathcal{R}e_p^{\text{crit}} \leq \mathcal{R}e \leq \mathcal{R}e_p^{\text{crit}} + 30$. The azimuthal waviness in these narrow gap cases is thus clearly driven by the axial shear in the azimuthal velocity. Further note that the height of the "harmonic ridge" decreases as η decreases from 0.85 to 0.7, a result that persists for smaller values of η, as described in Sec. III B. Moreover, Figure 5(d) also shows that along the "harmonic ridge" $k_s = 0$, the growth rate Im(ω_s) reaches a maximum in a small "island" of instability around $\mathcal{R}e \approx 140$ and then decreases with $\mathcal{R}e$. This feature will also be further addressed in Sec. III B. The azimuthal phase speed at mid-gap v_ϕ shown in Figure 6 also corroborates Figure 2(a). The phase speed along the "harmonic ridge" only weakly depends on n_s and $\mathcal{R}e$ and decreases from $v_\phi \sim 0.6$ for $\eta = 0.95$ to $v_\phi \sim 0.4$ for $\eta = 0.7$. On the "subharmonic hill," this phase speed remains smaller and eventually becomes negative as $\mathcal{R}e$ increases for $\eta = 0.7$ in Figure 6(d), indicating counter-propagating azimuthal waves with respect to the rotation of the inner cylinder.

B. Wide gap (small η) case

Results for smaller radius ratios are less clear. Figure 7 depicts the growth rates obtained for the complete solution and cases ①, ②, and ③ for $\eta = 0.55$, where $\mathcal{R}e_p^{\text{crit}} = 69.5$ and $k_p^{\text{crit}} = 3.15$. In this case, the complete secondary stability analysis in Figure 7(a) leads to a critical secondary instability with $k_s = k_p^{\text{crit}}/2$, $n_s^{\text{crit}} = 2$, $\mathcal{R}e_s^{\text{crit}} = 127.9$, i.e., $\epsilon_s^{\text{crit}} = 1.84$, and $v_\phi^{\text{crit}} = -0.03$. Though

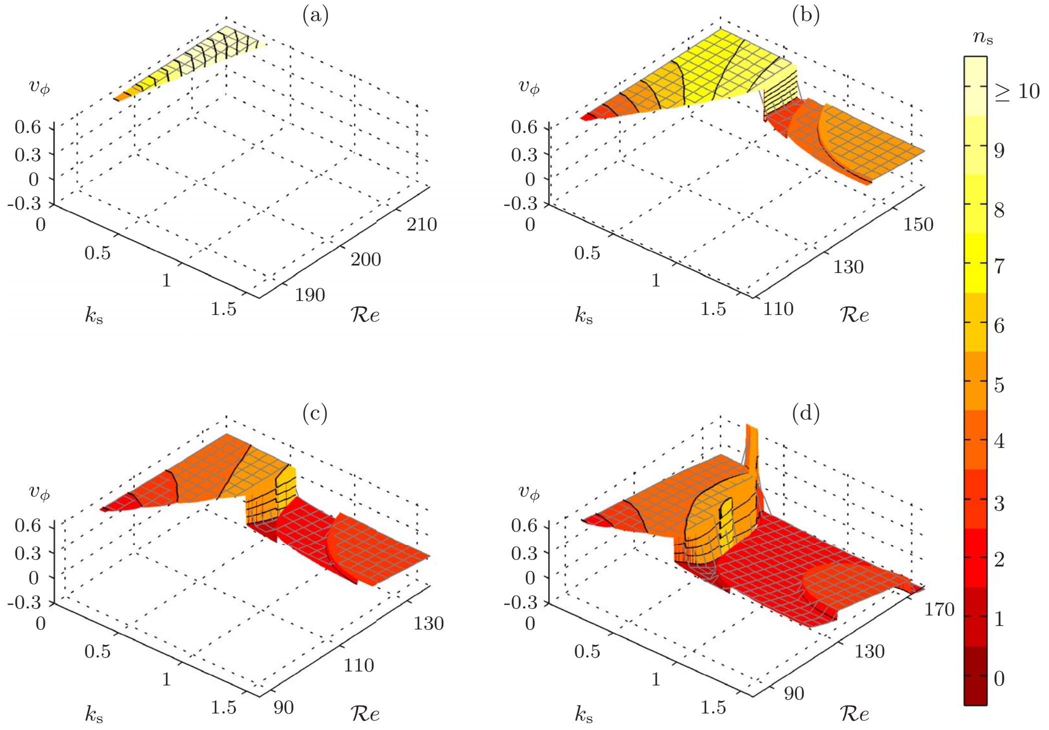

FIG. 6. Phase speed at mid-gap $v_\phi = \mathrm{Re}\,(\omega_s)\, r_{\mathrm{mid}} / (n_s \mathcal{R}e)$ and azimuthal wavenumber n_s (colorscale) of the secondary instability, as a function of the Floquet axial wavenumber k_s and Reynolds number Ta for the complete operator $\mathcal{A}$, with (a)–(d) and colorscale as in Figure 5.

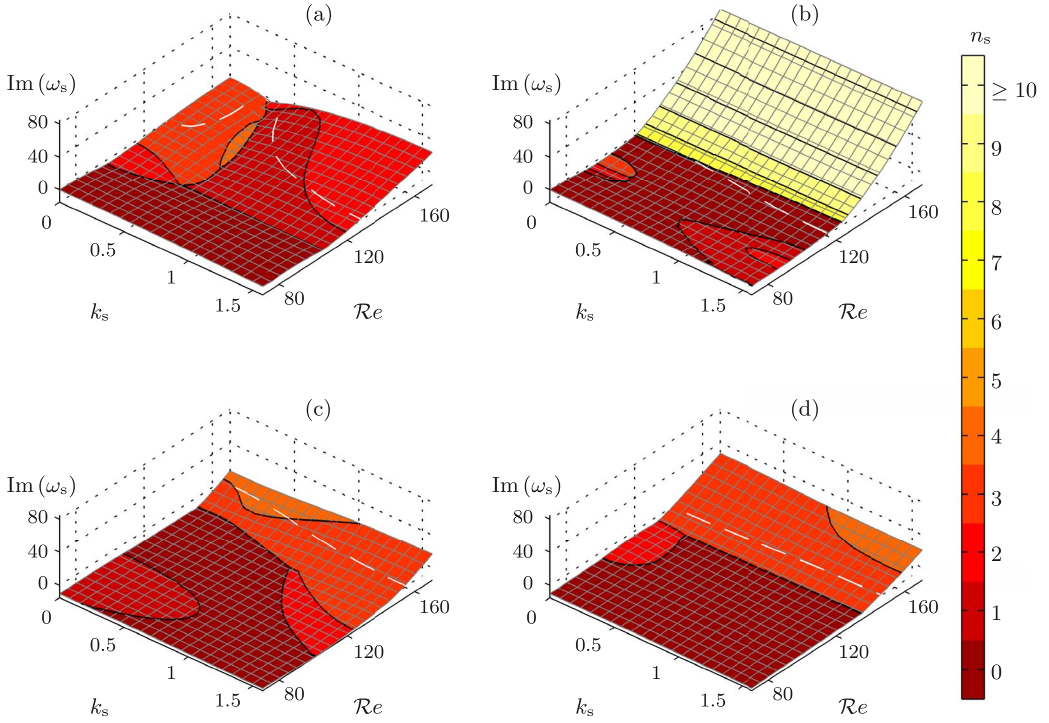

FIG. 7. Same as Figure 1, for $\eta = 0.55$. Note that the range of Reynolds numbers is double that in Figure 1.

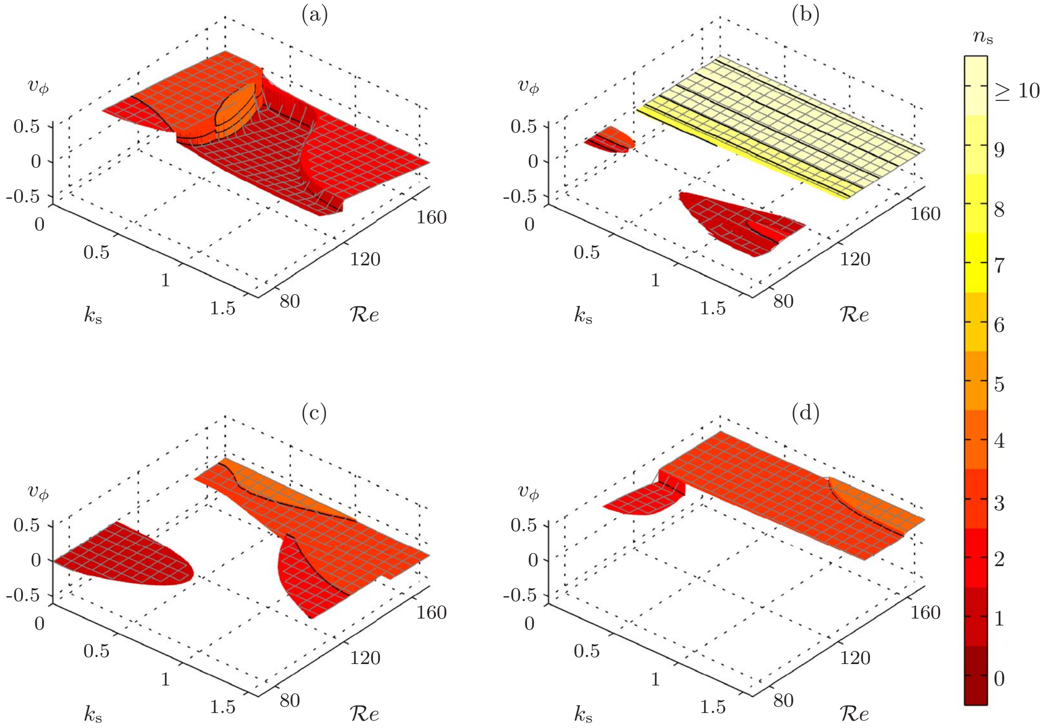

FIG. 8. Same as Figure 2, for $\eta = 0.55$.

$\epsilon_\mathrm{s}^\mathrm{crit}$ is larger than those for $\eta = 0.85$, it is not as large as values found by Jones.[20] Along the axial direction, based on k_s, this secondary instability is subharmonic, i.e., its axial wavelength is double the primary one. Along the azimuthal direction, this secondary instability exhibits a double wave ($n_\mathrm{s} = 2$). Based on v_ϕ^crit, it is evident in Figure 8(a) that upon the "subharmonic hill," v_ϕ actually changes from positive to negative values as the Reynolds number $\mathcal{R}e$ increases. So for secondary critical conditions, the azimuthal waviness is counter-propagating with respect to the rotation of the inner cylinder. For small values of η, the selection of a subharmonic mode, which has been called a "jet mode," has been reported experimentally[11] (for $\eta = 0.507$) and retrieved analytically[20] (for $\eta = 0.56$). Figure 7(a) also shows that the selection of the subharmonic mode is somewhat uncertain as it results from a competition between harmonic ($k_\mathrm{s} = 0$) and subharmonic ($k_\mathrm{s} = k_\mathrm{p}^\mathrm{crit}/2$) modes, both presenting very similar critical conditions.

Figures 7 and 8 demonstrate that none of the proposed mechanisms can by itself capture the features of the secondary dispersion relation, whether associated with harmonic or subharmonic modes. Whereas the complete case in Figures 7(a) and 8(a) obviously extends the evolution with η observed in Figures 5 and 6, with the presence of a "harmonic ridge" whose azimuthal waviness propagates at $v_\phi \approx 0.4$ and a "subharmonic hill" whose azimuthal waviness is slowly propagating or counter-propagating, these two features are no longer retrieved by the action of the azimuthal streaks (case ③) in Figures 7(d) and 8(d). The centrifugal force (case ①) in Figures 7(b) and 8(b) introduces a strong instability, nearly insensitive to k_s and presenting a high number ($n_\mathrm{s} \geq 8$) of non-propagating azimuthal waves. Although the radial jets (case ②) in Figures 7(c) and 8(c) sustain a subharmonic secondary mode, there is only a weak dependence on the axial wavenumber k_s, and the azimuthal phase speed at mid-gap v_ϕ is always negative. Thus, unlike the narrow gap case, there is no obvious explanation for the dynamics of the subharmonic or harmonic modes in the wide gap case. In other words, removing a single term among terms ①, ②, or ③ in the $\mathcal{A}$ operator (5) damps the instability associated with the "subharmonic hill" and "harmonic ridge."

Figure 9 depicts the amplitudes of the axial shears at mid gap in the radial and azimuthal velocity profiles from numerical simulations that are constrained to be axisymmetric for $\mathcal{R}e = 75$, 100, and

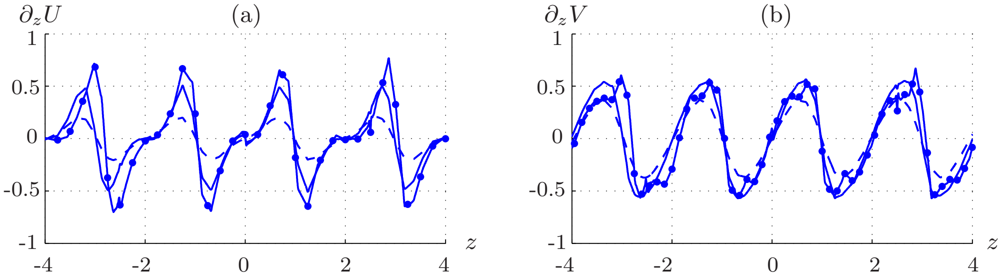

FIG. 9. Same as Figure 4, for $\eta = 0.55$, at Reynolds number $\mathcal{R}e = 75$ (dashed lines), 100 (solid lines) and 140 (solid lines with dots). Note that $\mathcal{R}e_{\mathrm{p}}^{\mathrm{crit}} = 69.5$.

140, i.e., $\epsilon = 1.08$, 1.44, and 2.01, respectively, for $\eta = 0.55$. It is evident that as the Reynolds number increases towards its critical value $\mathcal{R}e_{\mathrm{s}}^{\mathrm{crit}}$, the magnitude of the axial shear in the radial velocity $\partial_z U$ is comparable to the magnitude of the axial shear in the azimuthal velocity $\partial_z V$, in contrast with the case $\eta = 0.85$ shown in Figure 4. The mechanism driving the waviness in these wide gap cases hence remains unclear. It is likely a combination of several mechanisms, none of which can clearly be isolated using this approach.

Figure 10 sheds further light on the competition between harmonic and subharmonic secondary instabilities as the gap becomes larger, i.e., η decreases. First, it is evident in Figures 5(d) and 10(a) that the "harmonic ridge" actually presents a local maximum for the growth rate as a function of the Reynolds number, an "island of instability." As a corollary, the harmonic secondary mode returns to stability ($\mathrm{Im}(\omega_{\mathrm{s}}) < 0$) as the Reynolds number increases beyond this maximum (note that in Figure 10 the Reynolds number extends over a larger range than in Figures 5(b) and 5(c)). This restabilization of the "harmonic ridge" could account for the disappearance of the azimuthal waviness and return to the axisymmetric Taylor vortices that has been observed experimentally[23] and numerically[22] as the Reynolds number is further increased above its critical value $\mathcal{R}e_{\mathrm{s}}^{\mathrm{crit}}$ for $\eta \sim 0.75 - 0.78$. Second, in Figures 5(d), 10(a), and 10(b), critical conditions for harmonic and subharmonic modes are very similar. The selection of the harmonic mode in Figure 5(d) and subharmonic one in Figures 10(a) and 10(b) is therefore likely to be very sensitive to the assumptions behind the secondary stability analysis. It should be noted though that the "subharmonic hill" remains a well established feature associated with a monotonic increase of the growth rate with the Reynolds number, whereas the variation with $\mathcal{R}e$ along the "harmonic ridge" displays an "island" of faint instability. Thus, a subharmonic instability will always eventually occur as $\mathcal{R}e$ is increased, though this is less clear for a harmonic mode.

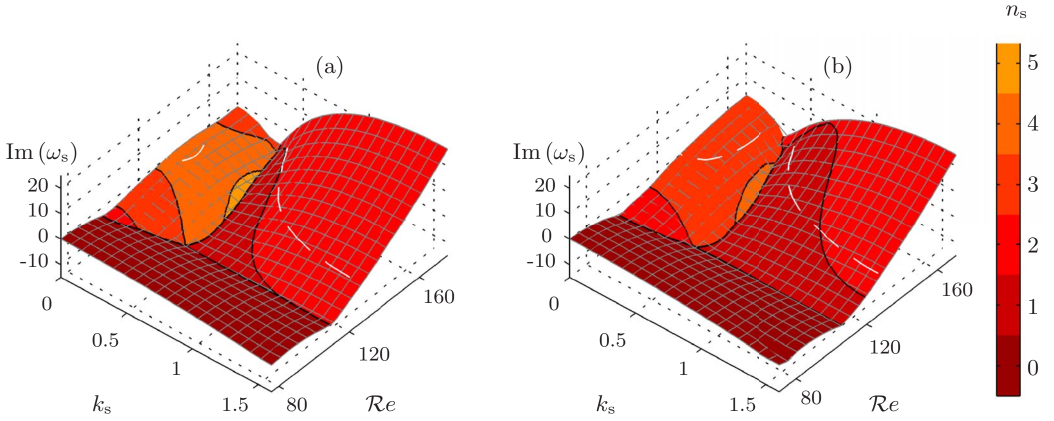

FIG. 10. Same as Figure 5, (a) $\eta = 0.65$, leading to $\mathcal{R}e_{\mathrm{s}}^{\mathrm{crit}} = 126.8$, $\epsilon_{\mathrm{s}}^{\mathrm{crit}} = 1.69$, $n_{\mathrm{s}} = 2$, and $v_\phi = -0.026$. (b) $\eta = 0.55$, leading to $\mathcal{R}e_{\mathrm{s}}^{\mathrm{crit}} = 127.9$, $\epsilon_{\mathrm{s}}^{\mathrm{crit}} = 1.84$, $n_{\mathrm{s}} = 2$, and $v_\phi = -0.029$.

IV. MORE DISCUSSION AND CONCLUSIONS

Figure 11 summarizes the critical conditions computed using the Floquet analysis as a function of the radius ratio, $0.5 \leq \eta \leq 0.97$. The primary and secondary critical Reynolds numbers, $\mathcal{R}e_{\mathrm{p}}^{\mathrm{crit}}$ and $\mathcal{R}e_{\mathrm{s}}^{\mathrm{crit}}$, respectively, and the ratio $\epsilon_{\mathrm{s}}^{\mathrm{crit}} = \mathcal{R}e_{\mathrm{s}}^{\mathrm{crit}}/\mathcal{R}e_{\mathrm{p}}^{\mathrm{crit}}$ are depicted in Figures 11(a) and 11(b). Basic features of the secondary wavy structures at the secondary threshold are depicted in Figure 11(c) for the axial and azimuthal wavenumbers and Figure 11(d) for the azimuthal wave speed. The secondary axial wavenumber is obtained as $k_{\mathrm{s}}^{\mathrm{crit}} + j_{\max} k_{\mathrm{p}}^{\mathrm{crit}}$, with $j_{\max}$ the index of the most energetic j-component of the Floquet vector in expansion (3). The azimuthal wave speed is compared to the velocity of the purely azimuthal flow $v_l(r_c)$, evaluated at the centers of the Taylor vortices. The position (r_c, z_c) in a meridional plane of such a center is obtained as a point where both the radial and axial velocities of the Taylor vortices vanish, i.e., $u_p(r_c) \times \exp(\mathrm{i}k_{\mathrm{p}}^{\mathrm{crit}} z_c) = w_p(r_c) \times \exp(\mathrm{i}k_{\mathrm{p}}^{\mathrm{crit}} z_c) = 0$. The shift from narrow gap (large η) to the wide gap (small η) cases occurs for $0.68 < \eta < 0.69$, where the secondary instability evolves from harmonic ($k_{\mathrm{s}} = 0$) for the narrow gap (large η) case to subharmonic ($k_{\mathrm{s}}^{\mathrm{crit}} = k_{\mathrm{p}}^{\mathrm{crit}}/2$) for the wide gap (small η) case (Figure 11(c)). This change is associated with a decrease of the azimuthal wavenumber to 2 and eventually 1, and the azimuthal waviness becomes counter-propagating, i.e., $v_\phi = \mathrm{Re}\left(\omega_{\mathrm{s}}^{\mathrm{crit}} r_{\mathrm{mid}}\right) / (n_{\mathrm{s}}\mathcal{R}e) < 0$. This shift induces a gradual increase of the critical secondary Reynolds number $\mathcal{R}e_{\mathrm{s}}^{\mathrm{crit}}$ and ratio $\epsilon_{\mathrm{s}}^{\mathrm{crit}}$, not a sharp increase as previously reported.[20]

Figure 11(b) shows that for η below 0.7, the gap between the primary and secondary critical conditions becomes fairly large, with $\epsilon_{\mathrm{s}}^{\mathrm{crit}} \sim 2$. Moreover, the Reynolds numbers covered by the secondary stability analyses for $\eta = 0.85$ in Figures 1 and 2 and for $\eta = 0.55$ in Figures 7 and 8 range over $1 < \epsilon < 1.47$ and $1 < \epsilon < 2.45$, respectively. Of course, this departure affects the validity of the weakly nonlinear approximation used to compute the saturated nonlinear state of the primary instability used in the base flow, Eq. (2). Two effects excluded from the present analysis can impact the secondary stability analysis, particularly for $\eta < 0.7$. First, slow modulations along the axial direction of the Taylor vortices have not been taken into account in their evaluation. The

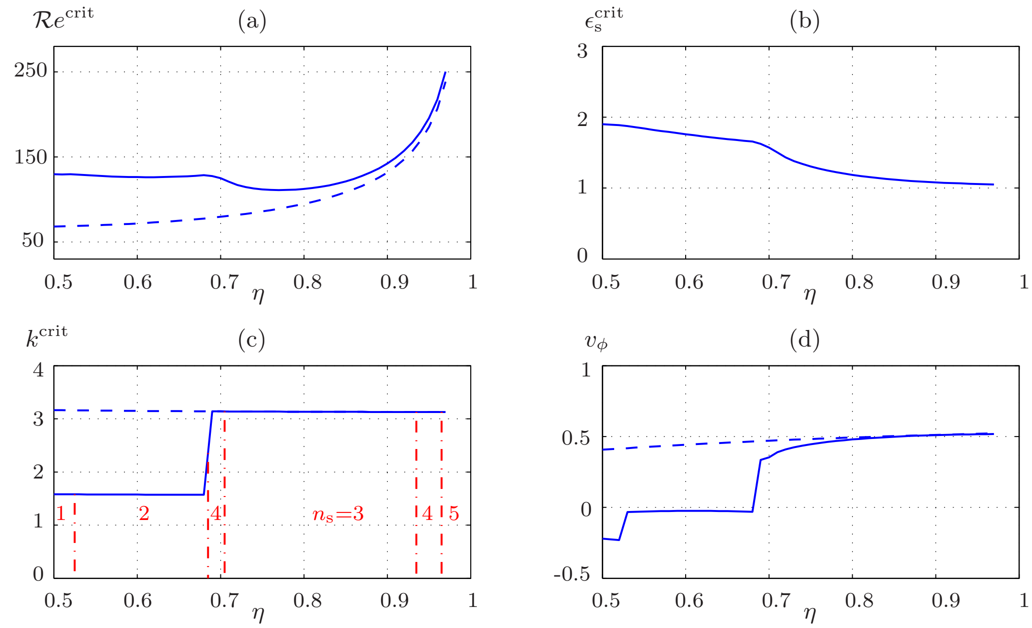

FIG. 11. Secondary critical conditions as functions of the radius ratio η, for $0.5 \leq \eta \leq 0.97$. (a) Primary and secondary critical Reynolds numbers, $\mathcal{R}e_{\mathrm{p}}^{\mathrm{crit}}$ (dashed line) and $\mathcal{R}e_{\mathrm{s}}^{\mathrm{crit}}$ (solid line) and (b) critical Reynolds number ratio $\epsilon_{\mathrm{s}}^{\mathrm{crit}}$. (c) Primary and secondary critical axial wavenumber, $k_{\mathrm{p}}^{\mathrm{crit}}$ (dashed line) and $k_{\mathrm{s}}^{\mathrm{crit}}$ (solid line) and secondary critical azimuthal wavenumber $n_{\mathrm{s}}^{\mathrm{crit}}$. (d) Azimuthal critical wave speed v_ϕ at mid gap (solid line) and velocity of the purely azimuthal flow at the center of a Taylor vortex (dashed line).

axial wavenumber of the saturated primary instability, which is kept fixed here at its critical value $k_\mathrm{p}^\mathrm{crit}$, could be modified in experimental or numerical realizations as an increasingly large band of wavenumbers becomes unstable as $\mathcal{R}e$ is increased above $\mathcal{R}e_\mathrm{p}^\mathrm{crit}$. The selection of a primary axial wavenumber $k_\mathrm{p} \neq k_\mathrm{p}^\mathrm{crit}$, by the finite-length of the system for instance, would modify the dispersion relations depicted in Figures 5 and 10 and Figure 11 accordingly. Allowing the primary axial wavenumber k_p to vary in the secondary stability problem (4), within the band of linearly unstable wavenumbers, would assess this modification. Along a similar line, Eckhaus instabilities could occur before secondary instabilities develop,[3] modifying the base flow upon which the secondary stability analysis is performed. Such features could be addressed by computing the Taylor vortices from an envelope equation rather than an amplitude equation. Beyond the added complexity of the stability analysis, it is very unlikely that this change would alter the main conclusions of this work on the mechanisms driving the waviness of the vortices. Second, the validity of the third order amplitude Eq. (1) and second order expansion (2) weakens as $\mathcal{R}e$ is increased above $\mathcal{R}e_\mathrm{p}^\mathrm{crit}$. The effects on the secondary stability analysis of higher harmonics in (2) are difficult to assess *a priori* and require proceeding to a higher order. Based on these shortcomings of the base flow (2), the dispersion relations for wide gaps depicted in Figure 10 should be considered with care. Furthermore, we do not include data for $\eta < 0.5$ in Figure 11, even though it is possible to carry out these calculations. Salient and robust features associated with monotonic increase of the growth rate $\mathrm{Im}(\omega_\mathrm{s})$ with the Reynolds number $\mathcal{R}e$, such as the "harmonic ridge" for large η and the "subharmonic hill" are reliable results of the secondary stability analysis in the sense that a modification of the base flow will quantitatively change the associated critical conditions but will not jeopardize these features. Fainter features such as the weak unstable "island" observed in Figures 5(d) and 10(a) along the "harmonic ridge" or the competition between the harmonic and subharmonic modes are likely to be qualitatively altered by a modification of the base flow.

In the case of large values of η (narrow gaps), the waviness of the vortices is unambiguously driven by the axial shear in the azimuthal velocity, generated by the alternate radial advection of high and low azimuthal momentum fluid close to the inner and outer cylinders, respectively. This mechanism becomes weaker as η is decreased below 0.70. This secondary transition is probably related to the instability of longitudinal streaks observed in plane shear flows.[25] It is important to note that the different character of the primary (centrifugal) and secondary (shear-driven) instabilities calls into question the approach to wavy vortex flow analysis using systems of amplitude equations satisfied by axisymmetric and non-axisymmetric perturbations to the purely azimuthal base flow, that has been used in the past,[24] as all these modes, which are driven by centrifugal forces, cannot capture the relevant physical mechanism. The results of our secondary stability analysis compare reasonably well with the numerical ones by Marcus[16] and theoretical ones by Jones.[20] At $\eta = 0.875$ and imposing $k_\mathrm{p} = 2.09$, $n_\mathrm{s} = 6$, and $\epsilon_\mathrm{s} = 2.063$, Marcus observed a harmonic secondary instability with $v_\phi = 0.376$. For $0.78 < \eta < 1$ and imposing harmonic instabilities with $k_\mathrm{p} = 3.13$, the secondary critical Reynolds numbers $\mathcal{R}e_\mathrm{s}^\mathrm{crit}$ and phase speeds v_ϕ computed by Jones[20] are similar to the ones obtained here, though Jones' most unstable azimuthal wavenumber is $n_\mathrm{s} = 1$. For $0.65 < \eta < 0.78$, Jones also observed some features retrieved in the present analysis such as the restabilization of the secondary instability as the Reynolds number is increased, the move to very low azimuthal phase speeds and the appearance of subharmonic modes. Although both approaches lead to azimuthal waviness related to the "harmonic ridge" for $\eta > 0.8$, the explanations concerning the underlying mechanism differ, as described in the Introduction. The results presented here clearly favor the explanation provided by Jones[20] and previously suggested by Davey *et al.*[24]

In the case of small values of η (wide gaps), no clear mechanism explaining the complete dispersion relation has been isolated using the approach developed here. To state it differently, all three mechanisms, i.e., the centrifugal force, the azimuthal streaks, and the radial jets, appear to be necessary for the harmonic or subharmonic secondary instability to develop. Concerning the numerical and experimental observations of these modes, their potential subharmonic character implies that their axial wavelength is the double that of the primary one. As a consequence, axial confinement in finite-length Taylor–Couette cells is likely to be even more critical to the occurrence of these modes than it is for harmonic secondary wavy vortices.

To conclude, whereas the mechanism driving the waviness for large values of η (narrow gaps) has clearly been identified as the azimuthal shear along the axial direction, a thorough and accurate analysis in the case of small values of η (wide gaps) is clearly beyond the reliable capability of the weakly nonlinear approximation adopted here and requires further numerical and experimental investigation.

[1] G. I. Taylor, "Stability of a viscous liquid contained between two rotating cylinders," Phil. Trans. R. Soc. A **223**, 289 (1923).
[2] M. A. Dominguez-Lerma, G. Ahlers, and D. S. Cannell, "Marginal stability curve and linear growth rate for rotating Couette–Taylor flow and Rayleigh–Bénard convection," Phys. Fluids **27**(4), 856 (1984).
[3] M. A. Dominguez-Lerma, D. S. Cannell, and G. Ahlers, "Eckhaus boundary and wave-number selection in rotating Couette–Taylor flow," Phys. Rev. A **34**(6), 4956 (1986).
[4] D. Coles, "Transition in circular Couette flow," J. Fluid Mech. **21**, 385 (1965).
[5] J. A. Cole, "Taylor vortex instability and annulus-length effects," J. Fluid Mech. **75**, 1 (1976).
[6] G. S. Bust, B. C. Dornblaser, and E. L. Koschmieder, "Amplitudes and wavelengths of wavy Taylor vortices," Phys. Fluids **28**, 1243 (1985).
[7] C. D. Andereck, S. S. Liu, and H. L. Swinney, "Flow Regimes in a circular Couette system with independently rotating cylinders," J. Fluid Mech. **164**, 155 (1986).
[8] W. S. Edwards, S. R. Beane, and S. Varma, "Onset of wavy vortices in the finite-length Couette–Taylor problem," Phys. Fluids A **3**(6), 1510 (1991).
[9] S. T. Wereley and R. M. Lueptow, "Azimuthal velocity in supercritical circular Couette flow," Exp. Fluids **18**, 1 (1994).
[10] S. T. Wereley and R. M. Lueptow, "Spatio-temporal character of non-wavy and wavy Taylor–Couette flow," J. Fluid Mech. **364**, 59 (1998).
[11] A. Lorenzen, G. Pfister, and T. Mullin, "End effects on the transition to time-dependent motion in the Taylor experiment," Phys. Fluids **26**, 10 (1983).
[12] E. Serre, M. A. Sprague, and R. M. Lueptow, "Stability of Taylor–Couette flow in a finite-length cavity with radial through-flow," Phys. Fluids **20**, 034106 (2008).
[13] C. A. Jones, "Nonlinear Taylor vortices and their stability," J. Fluid Mech. **102**, 249 (1981).
[14] G. Ahlers, D. S. Cannell, and M. A. Dominguez-Lerma, "Possible mechanism for transition in wavy Taylor-vortex flow," Phys. Rev. A **27**, 1225 (1983).
[15] G. P. King, Y. Li, W. Lee, H. L. Swinney, and P. S. Marcus, "Wave speeds in wavy Taylor-vortex flow," J. Fluid Mech. **141**, 365 (1984).
[16] P. S. Marcus, "Simulation of Taylor–Couette flow. Part 2. Numerical results for wavy vortex flow with one travelling wave," J. Fluid Mech. **146**, 65 (1984).
[17] W. Schröder and H. B. Keller, "Wavy Taylor-vortex flow via multigrid-continuation methods," J. Comp. Phys. **91**, 197 (1990).
[18] A. Akonur and R. M. Lueptow, "Three-dimensional velocity field for wavy Taylor–Couette flow," Phys. Fluids **15**, 947 (2003).
[19] K. Park and K. Jeong, "Stability boundary of the Taylor vortex flow," Phys. Fluids **27**, 2204 (1984).
[20] C. A. Jones, "The transition to wavy Taylor vortices," J. Fluid Mech. **157**, 135 (1985).
[21] U. Gerdts, J. von Stamm, Th. Buzug, and G. Pfister, "Axisymmetric time-dependent flow in the Taylor–Couette system," Phys. Rev. E **49**, 4019 (1994).
[22] J. Antonijoan and J. Sánchez, "On stable Taylor vortices above the transition to wavy vortices," Phys. Fluids **14**, 1661 (2002).
[23] T. T. Lim, Y. T. Chew, and Q. Xiao, "A new flow regime in a Taylor–Couette flow," Phys. Fluids **10**, 3233 (1998).
[24] A. Davey, R. C. DiPrima, and J. T. Stuart, "On the instability of Taylor vortices," J. Fluid Mech. **31**, 17 (1968).
[25] J. M. Hamilton, J. Kim, and F. Waleffe, "Regeneration mechanisms of near wall turbulence structures," J. Fluid Mech. **287**, 317 (1995).
[26] W. H. Finlay, J. B. Keller, and J. H. Ferziger, "Instability and transition in curved channel flow," J. Fluid Mech. **194**, 417 (1988).
[27] R. C. DiPrima, P. M. Eagles, and B. S. Ng, "The effect of radius ratio on the stability of Couette flow and Taylor vortex flow," Phys. Fluids **27**, 2403 (1984).
[28] G. Iooss, "Secondary bifurcations of Taylor vortices into wavy inflow or outflow boundaries," J. Fluid Mech. **173**, 273 (1986).
[29] K. Deguchi and S. Altmeyer, "Fully nonlinear mode competitions of nearly bicritical spiral or Taylor vortices in Taylor–Couette flow," Phys. Rev. E **87**, 043017 (2013).
[30] A. Davey, "The growth of Taylor vortices in flow between rotating cylinders," J. Fluid Mech. **14**, 336 (1962).
[31] T. Herbert, "Secondary instabilities of boundary layers," Annu. Rev. Fluid Mech. **20**, 487 (1962).
[32] J. M. Vanel, R. Peyret, and P. Bontoux, in *Numerical Methods for Fluid Dynamics II*, edited by K. W. Morton and M. J. Baines (Clarendon Press, Oxford, 1986), pp. 463–475.
[33] I. Raspo, S. Hughes, E. Serre, A. Randriamampianina, and P. Bontoux, "A spectral projection method for the simulation of complex three-dimensional rotating flows," Comput. Fluids **31**, 745 (2002).
[34] G. Fontaine, S. Poncet, and E. Serre, "Multidomain extension of a divergence-free pseudo-spectral algorithm for the direct numerical simulation of wall-confined rotating flows," Lect. Notes Comput. Sci. Eng. **95**, 261 (2014).
[35] D. Martinand, E. Serre, and R. M. Lueptow, "Absolute and convective instability of cylindrical Couette flow with axial and radial flows," Phys. Fluids. **21**, 104102 (2009).